JOURNAL OF GEOPHYSICAL RESEARCH, VOL. ???, XXXX, DOI:10.1029/,

An Explanation for the Effect of Clouds over Snow on the Top-of-Atmosphere Bidirectional Reflectance

Stephen R. Hudson and Stephen G. Warren

Department of Atmospheric Sciences, University of Washington, Seattle,

Washington, USA

Submitted to *Journal of Geophysical Research - Atmospheres*

13 February 2007

Revised version returned 20 June 2007

Accepted 27 June 2007

S. R. Hudson and S. G. Warren, Department of Atmospheric Sciences, University of Washington, Box 351640, Seattle, WA 98195-1640, USA. (hudson@atmos.washington.edu; sgw@atmos.washington.edu;)

Abstract.

It has been a long-standing puzzle why clouds, which should interact with solar radiation similarly to a thin layer of snow, have such a dramatic effect on the reflectance observed by satellites over snow-covered regions. The presence of a cloud over the snow strongly enhances the anisotropy of the scene, so that a cloud-over-snow scene appears darker than clear sky over snow when observed near nadir, but much brighter when observed at large zenith angles in the forward-reflected direction. By contrast, when a plane-parallel cloud is placed above a plane-parallel snow surface in a model, it slightly decreases the anisotropy of the system due to the cloud's smaller particles.

Using a parameterization for the directional reflectance from East-Antarctic snow, developed from extensive near-surface observations from a tower, we show that the unexpected effect of clouds over snow in this region is due to the non-plane-parallel nature of the snow surface, not to unexpected features of the clouds. The snow-surface roughness reduces the anisotropy of the reflected sunlight compared to that from a plane-parallel snow surface. Clouds, by hiding this roughness with a surface that is very smooth in units of optical depth, increase the anisotropy by bringing the system closer to the plane-parallel case. We use the surface parameterization to accurately model reflectance observations made from the tower over a ground fog and from the top of the atmosphere over cloud-covered snow by the MISR satellite instrument.

1. Introduction

Understanding the effect of clouds on the bidirectional reflectance distribution function (BRDF) of snow-covered areas of the planet is necessary for quantifying the effects of clouds on the Earth's radiation budget (ERB) and for measuring the ERB from space. Such an understanding could also help develop methods for identifying clouds over the polar regions from satellite observations, a task that is still the subject of much research [*Hatzianastassiou et al.*, 2001; *Li et al.*, 2003].

Clouds and snow are both made of water, so their absorption spectra are broadly similar. This is true for both ice clouds and liquid-water clouds, because the absorption spectra of ice and water approximately parallel each other across the solar spectrum [e.g. *Dozier*, 1989]; i.e., at wavelengths where electronic transitions and intramolecular vibrational transitions are the dominant absorption mechanisms. (The water and ice spectra diverge in the thermal infrared where rotation and lattice-vibrations become important [Figure 1 of *Irvine and Pollack*, 1968].) Viewed from above at most visible or near-infrared wavelengths, cloud-covered snow should therefore just resemble deeper snow, if there are no significant absorbers in the atmosphere between the cloud and the snow. The cloud particles, however, have effective radii $r_{\text{eff}} < 20$ μm, whereas surface snow grains are larger, with effective radii typically 50 μm for cold snow at the Antarctic surface, and much larger for melting snow. Because near-infrared albedo is higher for smaller particles, the broadband planetary albedo above a cloud over snow should be somewhat greater than that of clear sky over snow. The visible albedo should be unchanged. The effect on spectral albedo of putting a cloud over snow in a plane-parallel radiative transfer model

is shown in Figure 1b of *Masonis and Warren* [2001]; it is similar to the effect of a thin layer of fine-grained snow ($r_{\text{eff}} \sim 30$ μm) over a thick layer of 100-μm snow [Figure 4 of *Grenfell et al.*, 1994].

It has therefore been a long-standing puzzle that in nadir-viewing satellite pictures, cloud-covered snow is usually darker than clear sky over snow. *Welch and Wielicki* [1989] gave some examples from Landsat, one of which is reproduced in Figure 1. The entire upper half of this image contains snow-covered sea ice, but the lower-right portion of that ice is overlain by cloud, causing it to appear darker than the cloud-free areas with ice. *Welch and Wielicki* then used a Monte-Carlo model to show how clouds could lower the albedo over snow if they were tall and broken (essentially a 'trapping' effect as seen also for sastrugi in Figure 13 of *Warren et al.* [1998]). However, most clouds over snow do not have the height-to-width ratios required by *Welch and Wielicki*. Later *Nemesure et al.* [1994] compared Earth Radiation Budget Experiment (ERBE) measurements at the South Pole with surface identification of clear and cloudy scenes, showing that clouds do increase the planetary albedo over snow, in agreement with the plane-parallel model.

The darkening of the nadir view by clouds, also seen in AVHRR data by *Loeb* [1997], must therefore not indicate a reduced albedo, but instead be compensated by a brightening at larger viewing zenith angles. *Wilson and Di Girolamo* [2004] showed this to be true using measurements from the Multi-angle Imaging SpectroRadiometer (MISR), which observes the same scene nearly simultaneously at nine different viewing zenith angles. Clouds and the Earth's Radiant Energy System (CERES) measurements also give the same result [Figure 7 of *Loeb et al.*, 2005; Figure 3 of *Kato and Loeb*, 2005]. Some data from the case analyzed by *Wilson and Di Girolamo* [2004] are shown in Figure 2. These

show the bidirectional reflectance factor (a scaled reflectance that will be defined explicitly in Section 4) of the same scene, measured by MISR at different viewing angles. The scene consists of snow-covered sea ice in the Beaufort Sea, north of Alaska. The darkest areas are open water exposed in leads. Near the center of the images, a large floe is visible under mostly clear skies; the area in the left half of the images is overcast, with some leads still visible at nadir through the thin cloud. When observed at nadir (top panel) the cloudy area appears darker than the clear area, but when forward-scattered light is viewed in the lower panel, the clouds appear much brighter than the surface.

However, resolving one puzzle introduced another puzzle. In general, smaller particles are less forward-scattering than larger particles, so their asymmetry factors are lower. Putting a plane-parallel cloud, especially an ice cloud, over plane parallel snow in a radiative transfer model therefore slightly enhances the nadir reflection and reduces the forward reflectance peak, just the opposite of what is observed.

Explaining the observed effect of clouds on the reflected radiance field has proven difficult. *Welch and Wielicki* [1989] examined only near-nadir radiances and albedos, and therefore saw only that areas where clouds covered the snow were darker than cloud-free areas nearby. They attributed this darkening to increased absorption due to multiple scattering between the cloud and the surface giving the surface more opportunities to absorb the light, but this explanation does not explain the latter observation that cloudy areas are brighter than the cloud-free areas when viewed at large zenith angles. *Kato and Loeb* [2005] were unable to explain their observations from CERES using a plane-parallel radiative transfer model with a variety of particle scattering phase functions. They left the question unanswered, but suggested the effect may be due to surface roughness. Here we

present an argument for the surface-roughness explanation. In particular, we suggest that polar clouds, which are often stratiform and/or optically thin, present a surface that is, optically, much smoother than the snow surface, thus masking the effect that snow-surface roughness has on the BRDF of snow.

2. The Effect of Surface Roughness on the BRDF of Snow

Polar snow surfaces are usually rough, primarily due to wind erosion. In this paper, we focus on observations from the East Antarctic Plateau; Figure 3 shows a typical view of the rough snow surface found in this area. The surface features visible in Figure 3 are called sastrugi, and they are typically elongated, with their long dimensions aligned parallel to the direction the wind was blowing when they formed. The photograph was taken at Dome C (75°S, 123°E), where the standard deviation of surface elevation measurements made every 20 or 50 cm along several 20- to 35-meter lines was 2.3 cm, and where the highest sastrugi were 6 to 8 cm above the mean surface. The snow surface on many parts of the East Antarctic Plateau is rougher than at Dome C as a result of stronger winds.

We now consider the effect surface roughness has on the directional reflectance from a snow surface. Three-dimensional modelling of the radiative transfer in a snow pack with surface height variations similar to those found on polar snowpacks remains computationally challenging due to the large optical depth of the snow in the rough layer (just 1 cm of snow has an optical depth of more than 50). Nevertheless, we can gain an understanding of the effect of the roughness, at least qualitatively, without such modelling.

The simplest way to understand the effect is to consider how surface roughness affects what an observer sees when looking at a snow surface illuminated primarily by

direct-beam radiation with a non-zero solar zenith angle (Figure 4). When observing light coming from the direction of the solar azimuth, the observer will see the shaded or shadowed sides of roughness elements. When the observer looks at small viewing zenith angles (nearly straight down), significant areas of the snow between roughness elements and even some of the sunlit sides of the elements will be seen, but as the viewing zenith angle increases the fraction of the field of view occupied by the shaded sides of roughness elements will increase. The area of each roughness element that is shadowed will depend on both the geometry of the roughness elements and the solar zenith angle. For a given geometry, the shadowed area will increase with solar zenith angle once a critical solar zenith angle is reached; below that critical zenith angle (where the solar elevation angle is equal to the largest slope on the shaded side), the roughness element produces no shadowed area. Regardless of the solar zenith angle, all parts of the shaded side of the element will receive less incident energy per unit area than a flat surface would. The result is that surface roughness reduces the forward-reflected intensity, relative to that from an identical, flat snow surface. This effect is greater at larger viewing zenith angles, and larger solar zenith angles.

Similarly, when an observer looks directly away from the sun, at backward-reflected light, some part of the field of view will be occupied by the sunlit sides of the roughness elements. These sides will appear brighter than a flat snow surface because they receive more incident energy per unit area since the incident angle is locally reduced. Again, the effect will be greater at larger viewing zenith angles because the sunlit sides of elements will occupy a larger fraction of the field of view. This effect is also greater at larger solar zenith angles because the cosine changes more rapidly with angle for angles closer

to 90°. The effect is somewhat complicated by the fact that the viewing zenith angle is also locally different when viewing a roughness element, so variations in the BRDF of the snow with viewing angle may cause the intensity difference to differ from what would be expected from the difference in incident angle cosines. However, the increase in incident energy probably overwhelms changes in the BRDF, except at small solar zenith angles. The effects of sastrugi on the BRDF of the snow are quite apparent in the photographs shown in Figure 4.

Observational and modelling studies support the idea that snow-surface roughness has an effect on the directional reflectance from the snow. *Warren et al.* [1998] used directional reflectance observations from the South Pole, where the solar zenith remains nearly constant during a day as its azimuth changes, to show that the forward reflectance peak was reduced and the backward reflectance was enhanced when the solar azimuth was perpendicular to the long axis of the sastrugi (which are well-aligned at the South Pole due to a fairly constant wind direction), compared to when the two were parallel. Variations in the directional reflectance with the sun-sastrugi angle increased with viewing and solar zenith angles. *Leroux and Fily* [1998] and *O'Rawe* [1991] both modeled the reflectance from a snow surface with highly idealized sastrugi by combining the modeled BRDF of a flat snow surface with the shadowing and intercepting effects of the rough surface. Both of these modelling studies showed that the roughness reduces the forward scattering and enhances the backscattering, but the magnitude of the modeled effect was too large, compared to observations, likely because of the idealized geometry used to describe the sastrugi.

Loeb et al. [1998] used a three-dimensional Monte Carlo model to compare the reflectance of overcast scenes from plane-parallel clouds to that from clouds with cloud-top height variations. Their results show that the presence of cloud-top height variations reduces the forward reflectance, by up to 30% in their cases, and, in some cases, slightly enhances the backward reflectance, by up to 10%. Their optical depth variations were far smaller than those on the Antarctic snow surface, but the results are not directly comparable since their clouds were underlain by a black surface, emphasizing the low-order scattering. Nevertheless, these results again show that roughness reduces forward reflectance and enhances backward reflectance.

To get a sense of the magnitude of the effect of snow-surface roughness on the directional reflectance of East-Antarctic snow, we can compare observations with plane-parallel modelling results. First we define the anisotropic reflectance factor (R), which we use to describe the directional reflectance:

$$R(\theta_\circ, \theta_\mathrm{v}, \phi) = \frac{\pi I_\mathrm{r}(\theta_\circ, \theta_\mathrm{v}, \phi)}{\int_0^{2\pi} \int_0^{\pi/2} I_\mathrm{r}(\theta_\circ, \theta_\mathrm{v}, \phi) \cos\theta_\mathrm{v} \sin\theta_\mathrm{v} \, \mathrm{d}\theta_\mathrm{v} \, \mathrm{d}\phi}. \quad (1)$$

Here, $\theta_\circ$ is the solar zenith angle; θ_v is the viewing zenith angle; ϕ is the relative azimuth angle, and I_r is the reflected radiance. An isotropic surface with any non-zero albedo has $R = 1$ at all angles.

The values of R for the snow at Dome C at wavelength (λ) 800 nm and solar zenith angle 70° are contoured in Figure 5 (top left). These values are from the parameterization presented in *Hudson et al.* [2006], which was developed from spectral observations of R at Dome C at 96 different solar zenith angles. These observations were made with a measurement footprint that was large enough to include a representative sample of surface

roughness features, thereby capturing the effect of the surface roughness. When we need to make comparisons to clear-sky values of R at angles that were not observed, we use the parameterization to interpolate between angles that were observed.

The other plots in Figure 5 show the ratio of R predicted by DISORT [*Stamnes et al.*, 1988], a plane-parallel radiative transfer model, for snowpacks composed of ice spheres, aggregate grains, or columns, to the values of R for the Dome C snow. All modelling was done with $\theta_\circ = 70^\circ$ and atmospheric layers appropriate for the clear, summertime, Dome C atmosphere at $\lambda = 800$ nm. The atmospheric layers were created using SBDART [*Ricchiazzi et al.*, 1998], as described in section 5.3 of *Hudson et al.* [2006]. The single-scattering properties of the ice spheres were calculated for $\lambda = 800$ nm using the Mie code of *Wiscombe* [1980]. The single-scattering properties of the aggregates and columns were calculated using an improved geometrics optics method [*Yang and Liou*, 1996]. The phase functions used in these calculations are shown in Figure 6. The scattering properties of the aggregates and columns are both for ice crystals with microscale roughness on their surfaces, which eliminates the halo peaks in the phase function. Using the scattering properties for particles without this roughness produces halos in the reflectance that are only rarely seen in the real snow, but otherwise causes no significant differences in the results. The radiance leaving the snow was calculated by DISORT on a $1^\circ \times 1^\circ$ grid; these were then averaged to simulate the coarser resolution of the observations.

For each of these possible phase functions, Figure 5 shows that the ratio of the plane-parallel reflectance to the observed reflectance is significantly greater than one at large forward-reflected angles, and somewhat less than one at large backward-reflected angles, consistent with the expected effect of removing surface roughness. Also, the difference

between the plane-parallel reflectance and the observed reflectance increases with solar zenith angle (not shown). With $\theta_\circ = 83^\circ$ the plane-parallel R is around twice as large as the observed R in the forward direction, and about 30% lower in the backward direction; but with $\theta_\circ = 60^\circ$ the differences between the plane-parallel and observed values of R are not much larger than the uncertainty in the observations. The snow grains at Dome C are mostly irregular aggregates, so it is not surprising that the aggregate model has the smallest error.

By performing these calculations at $\lambda = 800$ nm, where Rayleigh scattering and atmospheric gaseous absorption are both weak, we have minimized the possibility of errors due to an inaccurate specification of the atmospheric properties. The snow at the Dome C observation site had measured soot content between 0.5 and 3 nanograms of carbon per gram of snow [*Warren et al.*, 2006], so impurities are unlikely to be the cause of the difference between the model and observations. Our modelling does not account for possible near-field effects of the closely packed snow grains; however, as explained by *Warren* [1982] in section E5a, this is not likely to be a problem since most of the volume of a shell of thickness on the order of λ surrounding a snow grain is occupied by air, not other snow grains. We therefore think it is reasonable to suggest that most of the difference between the modeled aggregate snowpack reflectance and the observed reflectance is due to the surface roughness, indicating that for this wavelength and solar zenith angle, the roughness reduces the forward reflectance by about 40%, and enhances backward reflectance by about 10%.

3. The BRDF of Fog over a Rough Snow Surface

Now that we have illustrated the effect of surface roughness on the directional reflectance of snow, we examine what happens when a cloud is placed above the rough snow surface. To begin, we look at the case of a thin fog layer above the snow. We made directional reflectance observations in the presence of fog at Dome C on several occasions. In all cases the fog layer extended from the surface to about 20 m; so, from our observation location at 32 m above the surface, we were looking down at the top of a thin cloud over the snow. As shown in Figure 7, the fog caused a strongly enhanced forward peak, noticeable by eye; its effect at other angles was less dramatic, except for the presence of a glory around the antisolar point. The glory, as well as riming on the observation tower, indicated that the fog was composed of supercooled liquid water droplets. These cases provide for a convenient case study since we have direct observations of the anisotropic reflectance pattern above the fog, along with observations at similar solar zenith angles without fog.

A representative reflectance observation above the fog is shown in Figure 8, along with the reflectance from the snow surface under a clear sky for the same solar zenith angle and wavelength; the relative difference caused by the fog is also shown. The addition of the fog has a qualitatively similar effect on the anisotropic reflectance factor to the removal of surface roughness; that is, it enhances the forward reflectance, by over 60% at large viewing angles, and reduces the backward reflectance, by about 20% at large viewing angles.

This similarity is more than coincidence. The thin fog, with an optical depth much less than one, presents an optically smooth surface, with optical depth variations that are

tiny compared to those on the snow surface; the standard deviation of the snow surface height, 2.3 cm, corresponds to an optical depth well over 100. The fog, formed in a very stable atmospheric layer, presents a surface that is also geometrically smooth, but the variations in optical depth are probably more important than those in geometrical depth. Either way, the smooth surface of the fog hides the rough surface of the snow, reducing the effects of the surface roughness on the directional reflectance, especially at large viewing zenith angles, where the optical slant path through the fog becomes significant.

If the fog is presenting a nearly plane-parallel surface, then we should be able to use DISORT to model this observation. However, since the fog is so thin, the surface reflectance is likely to remain important, so we must specify the correct surface BRDF, using the parameterization from *Hudson et al.* [2006], rather than modelling it as a plane-parallel surface or using an isotropic surface. By placing a cloud composed of 10-μm water spheres, with an optical depth of 0.05 above a surface with the parameterized snow-surface BRDF, we are able to match the fog-over-snow observation reasonably well as shown in Figure 9 (left and center). Except around the anti-solar point, where the modeled glory is probably too strong because of the uniform droplet size we used for the fog, the error in the model result is generally less than 10% and the strong enhancement of the forward peak seen in Figure 8 is modeled well. The angular separation of the glory fringes on a photograph during a different fog event at Dome C indicated an effective radius of between 7 and 8 μm. BRDF calculations were done for both $r_{\text{eff}} = 5$ μm and $r_{\text{eff}} = 10$ μm; the results were similar.

In order to get such accurate model results with this thin cloud, it is critical to use the correct surface BRDF, since, as illustrated by comparing a modeled clear-sky

reflectance for plane-parallel snow in Figure 9 (right) to the actual clear-sky reflectance in Figure 8 (center), modelling the surface as a plane-parallel snowpack grossly overestimates the forward reflectance at this large solar zenith angle. Therefore, modelling a fog above a plane-parallel snowpack would produce far too much forward reflectance. Of course the phase function of the fog particles is also important for the model; it was not possible to produce such accurate results with a fog composed of aggregate ice crystals. However, even when using an ice cloud, qualitatively correct effects, particularly an enhancement of the forward peak, are obtained, but errors in the side-scatter region are larger than with water drops.

4. The View from the Top of the Atmosphere

In the previous section we showed that the roughness of the snow surface is ultimately what leads to the observation that fog enhances the forward reflectance above snow. The fog case was a convenient one to use because of our observations, but the observations that inspired this work were made from the top of the atmosphere (TOA), and looked at thicker clouds. Now we show that this same argument works well for these observations also.

The TOA observations are often reported as a bidirectional reflectance factor (BRF). The BRF is similar to R, but with the denominator of Equation 1 replaced by the incident flux, so that an isotropic surface has a BRF at all angles equal to its albedo. Figure 10 shows the BRF near the forward-reflectance peak, measured by MISR at 866 nm from a region around Dome C. Some parts of this scene contain cloud, while other parts are clear. As expected for this viewing geometry, the cloudy areas appear significantly brighter than

the clear areas. The two black curves in Figure 11 show the MISR observations at all nine angles from the two points marked clear and cloudy in Figure 10. Here we can again see that, while the cloud appears brighter than the snow at large viewing zenith angles, it appears darker at near-nadir angles. (Unlike for the fog and plane-parallel snow, the cloud here appears brighter than the clear scene not only in the forward direction but also in the backward direction. This may be an effect of the different phase functions, or a result of the smaller solar zenith angle in this case. It could also simply be a result of comparing BRF with R; if the albedo of the cloudy scene is greater than that of the clear scene then a plot comparing R for these two scenes would have the cloudy curve shifted down relative to the clear curve. We do not have the necessary data to convert the MISR data to R or the surface data to BRF.)

Using DISORT, we modeled the TOA BRF for these two scenes. As for the results above, the model consisted of layers representative of the mean summertime Dome-C atmosphere above a surface with a specified BRDF. The surface BRDF was the product of our parameterization for R and the estimated albedo, both for 866 nm. Since we will now be comparing the BRF, rather than R, our estimate of albedo is important. The albedo was estimated by using SBDART to calculate the spectral albedo of snowpacks consisting of two layers, a 2.5 mm layer above a semi-infinite (optical depth 10,000) layer. The effective grain radius of each layer could be set to any multiple of 10 from 20 to 120 μm. The spectral albedo was then calculated for each combination of grain radii in the two layers, with layers above the snow representative of the Dome-C atmosphere containing a cloud that diffused the solar beam. The grain-size combination (40 μm above 90 μm) that resulted in the smallest root-mean-squared error when compared to

our observed albedo [Figure 6 of *Hudson et al.*, 2006], measured under diffuse incidence, was then used to calculate the clear-sky spectral albedo at solar zenith angles from 0° to 89°. The effect of surface roughness on albedo is expected to be much less than on reflected radiance [Section 8 of *Warren et al.*, 1998], so the use of a plane-parallel model here should not cause large errors.

The resulting modeled TOA BRF for the clear and cloudy scenes are shown in gray in Figure 11. These models used a solar zenith angle of 61.1°, the same as at the two locations at the time of observation. The cloudy scene was modeled with a single cloud layer with optical depth 10, composed of liquid water drops with radius 5 μm. The modeled BRF for the cloudy scene matches the observations quite well, and is not very sensitive to the cloud optical depth or droplet radius. The modeled BRF for the clear scene is also in fairly good agreement with the observations, though it does underestimate the BRF at larger forward angles by about 4%. The addition to the clear model of a layer of boundary-layer ice crystals or of stratospheric aerosols did not correct this error. It also did not help to perform an integration over the MISR channel, rather than using the central wavelength of 866 nm. It seems most likely that the difference between the modeled and observed clear-sky BRF is due mostly to variation in time or space of the snow-surface BRDF.

Figures 12 through 14 illustrate some of the spatial variability that sometimes exists in the snow-surface reflectance. Figure 12 shows a nadir image from MISR around Dome C on a clear day. At least two types of spatial variability appear in this image. The wavy patterns on the right side of the image are megadunes, surface features with amplitudes of a few meters and wavelengths of a few kilometers [*Fahnestock et al.*, 2000]. In the left half

of the image two areas with different reflectivities are visible, separated by a very distinct boundary. A likely explanation for this is that one of the regions has frost on the snow surface, while the other does not. As seen in Figure 13, dramatic changes in reflectance patterns due to frost have been observed while flying over Antarctica.

The observed BRF at all nine MISR angles at the four numbered locations in Figure 12 are shown in Figure 14, along with the modeled TOA BRF. In this case, the off-nadir model results lie in the low range of the observed spatial variability, except at two of the backward directions, where the model results are slightly less than the observations at any of these four locations.

The cases in Figures 10 through 14 show that our snow-surface reflectance parameterization may be used to model TOA BRF fairly accurately, but that there will be some errors in instantaneous comparisons due to spatial and temporal variability. That our measurement-based parameterization is appropriate for use in modelling satellite-observed reflectance, combined with the argument presented in Section 2 regarding the importance of surface roughness on the near-surface observations, suggests that the effect of surface roughness on satellite observations is similar to its effect on the near-surface observations, despite the satellite's larger footprint and much smaller angular field of view.

The orbital configuration of Terra, the spacecraft on which MISR flies, allows MISR to observe Dome C twice on most days, around 0000 and 1600 UTC (0800 and 0000 LST). The cases above were all from overpasses around 0000 UTC, and therefore all have solar zenith angles around 60° since they were all made in late December or January. As mentioned in Section 2, at these solar zenith angles, a plane-parallel snowpack composed of aggregate snow grains has almost the same anisotropy as the observed snowpack. There-

fore, when we model these MISR observations using a plane-parallel, aggregate-grain snow pack, the results have very similar anisotropy to what was observed by MISR; however, the resulting BRF is too high at all angles. Using larger aggregate grains would reduce the albedo, but would also likely increase the anisotropy. However, the better test of whether these scenes can be modeled with plane-parallel snow comes at larger solar zenith angles.

To look at this, we chose a clear scene from an overpass around 1600 UTC, when the solar zenith angle was 85°. Because Earth's curvature, which we do not account for, becomes important at large solar zenith angles, a solar zenith angle intermediate between 60° and 85° would probably be preferable, but is not available. In Figure 15 we compare two results for the modeled TOA BRF with the observed BRF. The solid gray curve, modeled using the observed surface, compares very well with the observation, with errors less than 10%, despite the large solar zenith angle. The largest errors occur at 26° and 46° in the backward direction, angles that may be affected by the shadow of the tower in our near-surface observations. The dashed gray curve, modeled using a plane-parallel snow pack composed of aggregate grains, shows much larger errors, especially near the forward peak, where the modeled BRF is nearly 30% too large. Again, this shows that the effects of the surface roughness become much more important as the solar zenith angle increases. We estimated the uncertainty caused by neglecting Earth's curvature by rerunning the observed-surface model with the optical depth of each atmospheric layer reduced so that the solar beam passed through the same optical depth in each layer as it would if the model accurately handled the curved geometry of the problem. The results with this simple correction differed by less than 0.5% from the results presented above.

The curvature would be much more important at a wavelength where light interacts more with the atmosphere.

5. Conclusions

The inability of plane-parallel snow-pack models, using a variety of phase functions, to reproduce the anisotropy observed in the reflected radiance field over the snow surface at Dome C, combined with the fact that the error from all of these models is qualitatively in agreement with the expected effect of neglecting surface roughness, strongly suggests that the snow-surface roughness present on the Antarctic Plateau significantly alters the directional reflectance from the snow. Its effect is primarily to reduce the intensity at forward-reflected directions and to increase the intensity at other angles. This effect increases with solar zenith angle, and may be negligible at Dome C for solar zenith angles less than about 60°. Providing an accurate quantitative value for the magnitude of the effect of the surface roughness is an undertaking that will have to wait for computing improvements to allow for three-dimensional modelling of a realistic rough snow surface.

Plane-parallel models are able to calculate the reflected intensity field above clouds over the snow at Dome C if they use a parameterization of the reflectance from the snow surface at Dome C as the lower boundary. We showed good agreement between calculated and observed reflectance, for both clear and cloudy scenes, both near the surface and at the top of the atmosphere. Such agreement was possible with the use of plane-parallel clouds, showing that the unexpected effects of having a cloud over the snow surface, a darkening of near-nadir views and brightening of forward-reflected views, is not caused by special properties of the clouds, but rather by the non-plane-parallel nature of the snow

surface. Placing a cloud above the rough snow surface simply hides the snow-surface roughness with a surface that is, in units of optical depth, nearly plane parallel.

Clouds over snow affect the reflected radiance field most strongly and consistently near the principal plane, especially at large viewing zenith angles in the forward-scattering direction. Therefore, future projects wishing to accurately identify clouds over polar regions would benefit from the ability to observe at these angles. Instruments such as MISR, which can observe the same location from multiple angles near the principal plane in a short period, are especially well-suited for polar cloud identification using reflected natural light; however, future versions would need a wider swath width to fully cover the polar regions. Multi-angle instruments provide other benefits as well, such as stereo imaging to identify clouds.

Finally, the agreement between modeled and MISR-observed bidirectional reflectance at the top of the atmosphere, using the parameterized snow surface as the lower boundary in the model, indicates that this parameterization may be successfully used to model observations from satellites of the area around Dome C. This shows that, despite the differences in footprint size and angular field of view between satellite and near-surface observations, these types of field observations of directional reflectance from Earth's surfaces can be valuable tools for analyzing and interpreting satellite data. The effect of the surface roughness in this case, which can be observed only by going far enough above the surface to observe a fairly large footprint, shows that designers of such field programs must take care to ensure their measurements are representative of the large-scale views of the region if their data are to be used in this way.

Acknowledgments.

Yu Xie and Ping Yang generously computed the ice crystal phase functions for us. Delphine Six provided the measurements of the surface-height variations from Dome C. Ronald Welch supplied Figure 1 and Nadine Nereson supplied Figure 13. Richard Brandt estimated the fog drop sizes from photographs of the glory, at the suggestion of James Spinhirne. MISR data were obtained from the NASA Langley Atmospheric Sciences Data Center. We thank Thomas Grenfell and Richard Brandt for their assistance and insights on this work. We also benefited from discussions with Larry Di Girolamo and Michael Wilson and from the helpful comments of three anonymous reviewers. This research was supported by National Science Foundation grants OPP-00-03826 and ANT-06-36993.

References

Dozier, J. (1989), Estimation of properties of alpine snow from landsat thematic mapper, *Adv. Space Res.*, *9*(1), 207–215, doi:10.1016/0273-1177(89)90487-0.

Fahnestock, M. A., T. A. Scambos, C. A. Shuman, R. J. Arthern, D. P. Winebrenner, and R. Kwok (2000), Snow megadune fields on the East Antarctic Plateau: extreme atmosphere-ice interaction, *Geophys. Res. Lett.*, *27*(22), 3719–3722, doi:10.1029/1999GL011248.

Grenfell, T. C., S. G. Warren, and P. C. Mullen (1994), Reflection of solar radiation by the Antarctic snow surface at ultraviolet, visible, and near-infrared wavelengths, *J. Geophys. Res.*, *99*(D9), 18,669–18,684, doi:10.1029/94JD01484.

Hatzianastassiou, N., N. Cleridou, and I. Vardavas (2001), Polar cloud climatologies from ISCCP C2 and D2 datasets, *J. Climate*, *14*(18), 3851–3862, doi:10.1175/1520-0442(2001)014<3851:PCCFIC>2.0.CO;2.

Hudson, S. R., S. G. Warren, R. E. Brandt, T. C. Grenfell, and D. Six (2006), Spectral bidirectional reflectance of Antarctic snow: Measurements and parameterization, *J. Geophys. Res.*, *111*(D18), D18106, doi:10.1029/2006JD007290.

Irvine, W. M., and J. B. Pollack (1968), Infrared optical properties of water and ice spheres, *Icarus*, *8*(1–3), 324–360, doi:10.1016/0019-1035(68)90083-3.

Kato, S., and N. G. Loeb (2005), Top-of-atmosphere shortwave broadband observed radiance and estimated irradiance over polar regions from Clouds and the Earth's Radiant Energy System (CERES) instruments on Terra, *J. Geophys. Res.*, *110*, D07202, doi:10.1029/2004JD005308.

Leroux, C., and M. Fily (1998), Modeling the effect of sastrugi on snow reflectance, *J. Geophys. Res.*, *103*(E11), 25,779–25,788, doi:10.1029/98JE00558.

Li, J., W. P. Menzel, Z. Yang, R. A. Frey, and S. A. Ackerman (2003), High-spatial-resolution surface and cloud-type classification from MODIS multispectral band measurements, *J. Appl. Meteorol*, *42*(2), 204–226, doi: 10.1175/1520-0450(2003)042<0204:HSRSAC>2.0.CO;2.

Loeb, N. G. (1997), In-flight calibration of NOAA AVHRR visible and near-IR bands over Greenland and Antarctica, *Int. J. Remote Sens.*, *18*(3), 477–490, doi: 10.1080/014311697218908.

Loeb, N. G., T. Várnai, and D. M. Winker (1998), Influence of subpixel-scale cloud-top structure on reflectances from overcast stratiform cloud layer, *J. Atmos. Sci.*, *55*(18), 2960–2973, doi:10.1175/1520-0469(1998)055<2960:IOSSCT>2.0.CO;2.

Loeb, N. G., S. Kato, K. Loukachine, and N. Manalo-Smith (2005), Angular distribution models for top-of-atmosphere radiative flux estimation from the Clouds and the Earth's Radiant Energy System instrument on the *Terra* satellite. Part I: Methodology, *J. Atmos. Oceanic Technol.*, *22*(4), 338–351, doi:10.1175/JTECH1712.1.

Masonis, S. J., and S. G. Warren (2001), Gain of the AVHRR visible channel as tracked using bidirectional reflectance of Antarctic and Greenland snow, *Int. J. Remote Sens.*, *22*(8), 1495–1520, doi:10.1080/01431160121039.

Nemesure, S., R. D. Cess, E. G. Dutton, J. J. DeLuisi, Z. Li, and H. G. Leighton (1994), Impact of clouds on the shortwave radiation budget of the surface-atmosphere system for snow-covered surfaces, *J. Climate*, *7*(4), 579–585, doi:10.1175/1520-0442(1994)007<0579:IOCOTS>2.0.CO;2.

O'Rawe, P. (1991), Monte Carlo models for the reflection of sunlight from rough snow surfaces: Suncups and sastrugi, Master's thesis, Univ. of Washington, Seattle, 521 pp.

Ricchiazzi, P., S. Yang, C. Gautier, and D. Sowle (1998), SBDART: A research and teaching software tool for plane-parallel radiative transfer in the Earth's atmosphere, *Bull. Amer. Meteor. Soc.*, *79*(10), 2101–2114, doi: 10.1175/1520-0477(1998)079<2101:SARATS>2.0.CO;2.

Stamnes, K., S.-C. Tsay, W. Wiscombe, and K. Jayaweera (1988), Numerically stable algorithm for discrete-ordinate-method radiative transfer in multiple scattering and emitting layered media, *Appl. Opt.*, *27*(12), 2502–2509.

Warren, S. G. (1982), Optical properties of snow, *Rev. Geophys. Space Phys.*, *20*(1), 67–89.

Warren, S. G., R. E. Brandt, and P. O'Rawe Hinton (1998), Effect of surface roughness on bidirectional reflectance of Antarctic snow, *J. Geophys. Res.*, *103*(E11), 25,789–25,807, doi:10.1029/98JE01898.

Warren, S. G., R. E. Brandt, and T. C. Grenfell (2006), Visible and near-ultraviolet absorption spectrum of ice from transmission of solar radiation into snow, *Appl. Opt.*, *45*(21), 5320–5334, doi:10.1364/AO.45.005320.

Welch, R. M., and B. A. Wielicki (1989), Reflected fluxes for broken clouds over a Lambertian surface, *J. Atmos. Sci.*, *46*(10), 1384–1395, doi:10.1175/1520-0469(1989)046<1384:RFFBCO>2.0.CO;2.

Wilson, M. J., and L. Di Girolamo (2004), The utilization of MISR for polar cloud modeling, in *Geoscience and Remote Sensing Symposium, 2004. IGARSS '04. Proceedings. 2004 IEEE International*, vol. 7, pp. 4361–4362, IEEE, doi: 10.1109/IGARSS.2004.1370114.

Wiscombe, W. J. (1980), Improved Mie scattering algorithms, *Appl. Opt.*, *19*(9), 1505–1509.

Yang, P., and K. N. Liou (1996), Geometric-optics-integral-equation method for light scattering by nonspherical ice crystals, *Appl. Opt.*, *35*(33), 6568–6584.

Figure 1. Landsat scene of partial cloud cover over sea ice in the Beaufort Sea, 71.0°N, 143.5°W, 12 October 1986. The solar elevation is 11°, solar azimuth is to the lower right of the frame. The shadow of the cloud is apparent as the dark band extending from lower left to upper right. The width of the frame is 185 km. Spatial resolution is 57 m. (Figure 4D of *Welch and Wielicki* [1989]; original photo supplied by R. Welch.)

Figure 2. Bidirectional reflectance factor (BRF) at 672 nm observed by two cameras on MISR over the Beaufort Sea on 4 June 2000 at 0708 UTC (block 8 of orbit 2460, data version number 23). The top panel shows the BRF observed near nadir and the bottom shows the BRF measured when looking at a zenith angle of 70.5°, 15° from the principal plane, in the forward direction. The grid is labeled in degrees of north latitude and west longitude. The local time at longitude 150°W was 2108, so the sun was in the northwest at zenith angle 78°; the direction of view in the lower image (also the direction of travel for the satellite) is towards the top of the page.

Figure 3. A photograph of a typical rough snow surface on the East Antarctic Plateau. The photograph is looking west from 32 m above the surface at Dome C; the sun is in the north.

Figure 4. Two photographs of the snow surface at the South Pole taken from 22 m above the surface at the same time, in early March, just before sunset. The one on the left was taken while facing away from the sun, showing that the sastrugi enhance backward reflectance. The one on the right was taken while facing the sun, showing that the sastrugi reduce forward reflectance. The

extremely large solar zenith angle and the wide spacing between sastrugi combine to make the effect very easy to see. The time of day was chosen so that the solar azimuth was approximately perpendicular to the long axis of the sastrugi, which also maximizes the effect.

Figure 5. The upper-left plot shows the anisotropic reflectance factor (R) of the snow at Dome C. The other plots show the ratio of R modeled with DISORT, using different shapes to represent the snow grains, to the values in the upper-left plot. All plots are for wavelength 800 nm and solar zenith angle 70°. Values are contoured as functions of viewing zenith angle, increasing with distance from the center, and relative azimuth angle, increasing clockwise from the top. Dots are located every 15° in both zenith (starting at 22.5°) and azimuth. Note the contour intervals vary within and between plots.

Figure 6. The three phase functions used in the modelling results shown in Figure 5. The solid line is the phase function for a 50-μm ice sphere, the dashed line is that for an aggregate ice crystal with maximum dimension of 200 μm, and the dotted line is that for a hexagonal column ice crystal with $a = 10$ μm and a length of 20 μm. The 0° to 10° region is enlarged in the inset, where the horizontal lines mark the maximum values.

Figure 7. A photograph showing the strongly enhanced forward peak caused by a thin fog layer over the snow at Dome C.

Figure 8. Observed R at Dome C with fog over the snow, R for the snow at Dome C with clear sky and no fog, and the relative difference caused by the fog (%). Observations are for $\theta_\circ = 82.7°$ and $\lambda = 800$ nm.

Figure 9. R modeled with DISORT for a thin, plane-parallel, liquid-water cloud immediately above a surface with the observed Dome C snow-surface BRDF, and the error of the model results relative to the fog-over-snow observation in Figure 8. Also shown is R modeled for a plane-parallel snowpack composed of rough aggregate snow grains under a clear sky. Both models used $\theta_\circ = 82.7°$ and $\lambda = 800$ nm.

Figure 10. The BRF at 866 nm observed by MISR near Dome C at 0006 UTC 17 January 2005 at viewing zenith angle 71° and relative azimuth angle near 30°. The two marked locations in this image, one with cloud cover and one with clear sky, were chosen for further analysis (see Figure 11). A visual observation of the sky from the surface indicates it was overcast at Dome C (DC) at this time. Some surface features are visible in the clear region in the higher-resolution nadir image. The interpretation of the brighter areas as cloud and darker areas as clear is also supported by the MODIS cloud mask. The grid is labeled in degrees of south latitude and east longitude. This case uses MISR data with version number 24.

Figure 11. Observed and modeled TOA 866-nm BRF at the clear and cloudy locations marked in Figure 10. The solar zenith angle is 61.1°. The relative azimuth is about 30° for positive viewing zenith angles (forward scattering) and 150° for negative viewing zenith angles (backscattering).

Figure 12. The near-nadir 866-nm BRF observed by MISR near Dome C at 2343 UTC 18 January 2004. The visibility of known surface features in the image and a coincident surface observation of the sky over Dome C both indicate that

the sky is clear in most, if not all, of the image. The wave-like features to the right are megadunes, large-scale features on the snow surface. The magnitude of the BRF variations are small (note the scale), but, to the left, two different snow types are clearly visible. The four numbered locations correspond to the observations plotted in Figure 14. The grid is labeled in degrees of south latitude and east longitude. This case uses MISR data with version number 22.

Figure 13. View from an airplane near Siple Dome, West Antarctica (82°S, 150°W), November 1994. The surface elevation is about 500 m. The streaks which appear dark in this photograph were later identified (on an oversnow traverse by snowmobile) as surface frost; viewed from the opposite direction they instead appear brighter than the intervening regions of snow. [The frost therefore probably has little effect on the albedo.] Photo by Nadine Nereson.

Figure 14. The four black curves show the 866-nm BRF observed by MISR at the four numbered locations in Figure 12. The gray curve is the modeled TOA 866-nm BRF. The solar zenith angle is about 63.5°.

Figure 15. The observed 866-nm BRF at 1607 UTC 22 January 2004 from a clear location near Dome C is shown in black. The solid gray curve is the modeled TOA 866-nm BRF using the surface parameterization. The dashed gray curve shows the modeled BRF using a plane-parallel surface composed of aggregate ice crystals. The solar zenith angle is 85.0°. This case uses MISR data with version number 22.

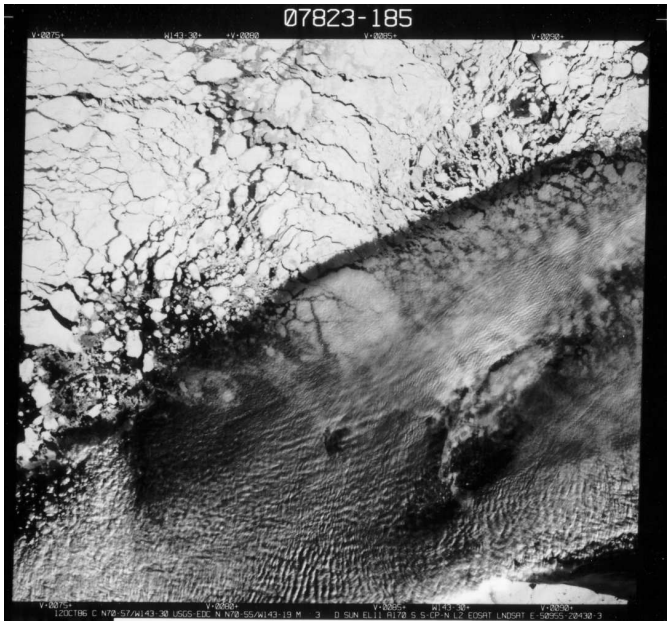

Figure 1. Landsat scene of partial cloud cover over sea ice in the Beaufort Sea, 71.0°N, 143.5°W, 12 October 1986. The solar elevation is 11°, solar azimuth is to the lower right of the frame. The shadow of the cloud is apparent as the dark band extending from lower left to upper right. The width of the frame is 185 km. Spatial resolution is 57 m. (Figure 4D of *Welch and Wielicki* [1989]; original photo supplied by R. Welch.)

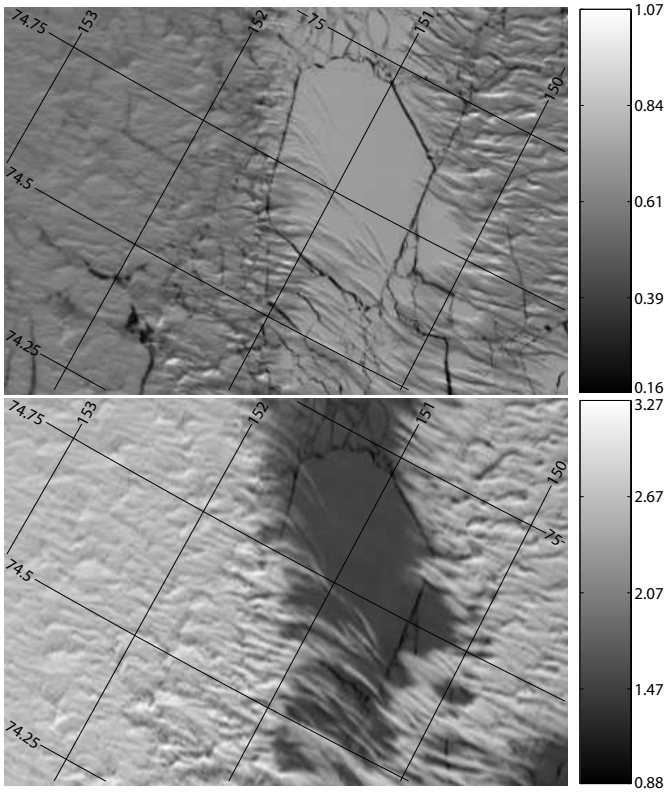

Figure 2. Bidirectional reflectance factor (BRF) at 672 nm observed by two cameras on MISR over the Beaufort Sea on 4 June 2000 at 0708 UTC (block 8 of orbit 2460, data version number 23). The top panel shows the BRF observed near nadir and the bottom shows the BRF measured when looking at a zenith angle of 70.5°, 15° from the principal plane, in the forward direction. The grid is labeled in degrees of north latitude and west longitude. The local time at longitude 150°W was 2108, so the sun was in the northwest at zenith angle 78°; the direction of view in the lower image (also the direction of travel for the satellite) is towards the top of the page.

Figure 3. A photograph of a typical rough snow surface on the East Antarctic Plateau. The photograph is looking west from 32 m above the surface at Dome C; the sun is in the north.

Figure 4. Two photographs of the snow surface at the South Pole taken from 22 m above the surface at the same time, in early March, just before sunset. The one on the left was taken while facing away from the sun, showing that the sastrugi enhance backward reflectance. The one on the right was taken while facing the sun, showing that the sastrugi reduce forward reflectance. The extremely large solar zenith angle and the wide spacing between sastrugi combine to make the effect very easy to see. The time of day was chosen so that the solar azimuth was approximately perpendicular to the long axis of the sastrugi, which also maximizes the effect.

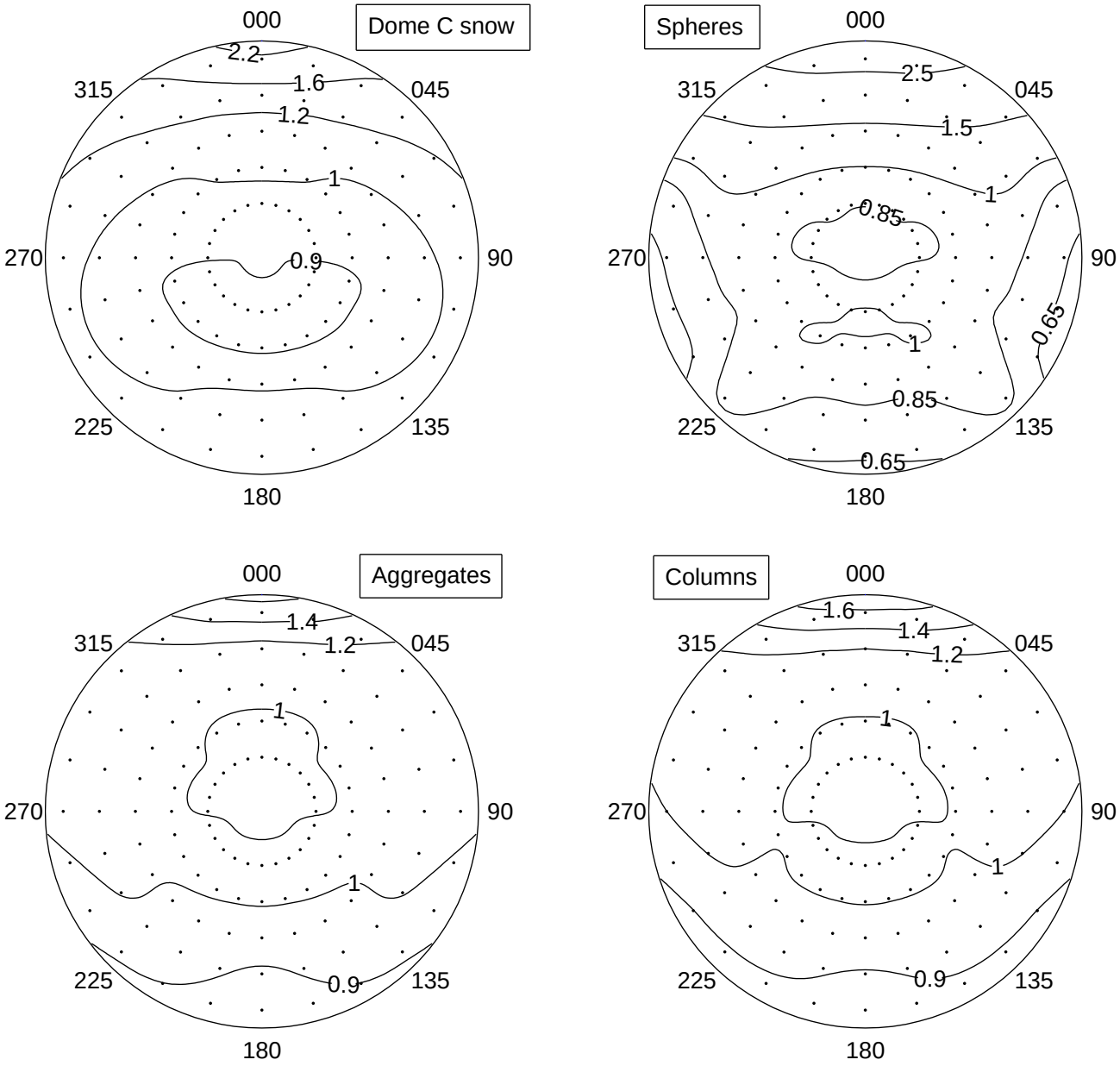

Figure 5. The upper-left plot shows the anisotropic reflectance factor (R) of the snow at Dome C. The other plots show the ratio of R modeled with DISORT, using different shapes to represent the snow grains, to the values in the upper-left plot. All plots are for wavelength 800 nm and solar zenith angle 70°. Values are contoured as functions of viewing zenith angle, increasing with distance from the center, and relative azimuth angle, increasing clockwise from the top. Dots are located every 15° in both zenith (starting at 22.5°) and azimuth. Note the contour intervals vary within and between plots.

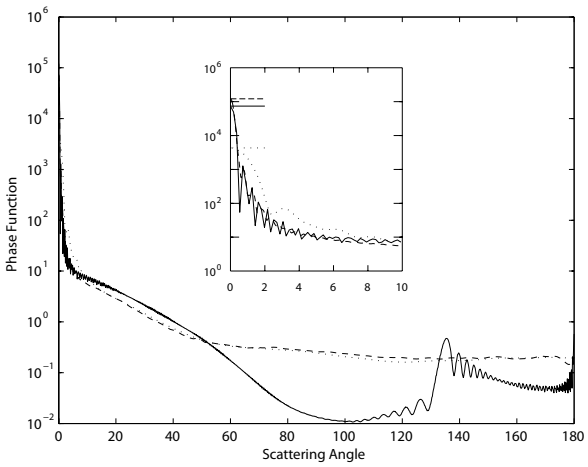

Figure 6. The three phase functions used in the modelling results shown in Figure 5. The solid line is the phase function for a 50-μm ice sphere, the dashed line is that for an aggregate ice crystal with maximum dimension of 200 μm, and the dotted line is that for a hexagonal column ice crystal with $a = 10$ μm and a length of 20 μm. The 0° to 10° region is enlarged in the inset, where the horizontal lines mark the maximum values.

Figure 7. A photograph showing the strongly enhanced forward peak caused by a thin fog layer over the snow at Dome C.

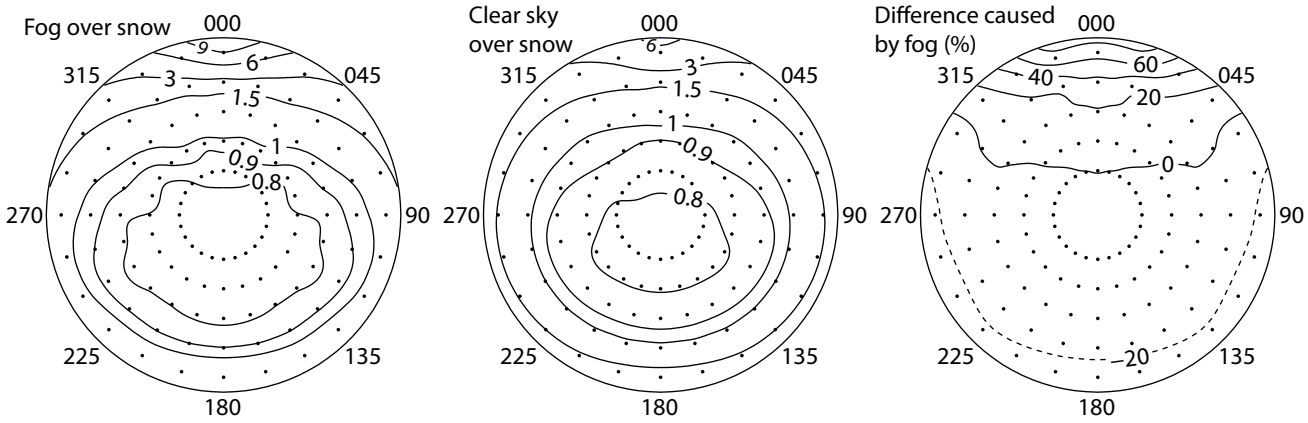

Figure 8. Observed R at Dome C with fog over the snow, R for the snow at Dome C with clear sky and no fog, and the relative difference caused by the fog (%). Observations are for $\theta_\circ = 82.7°$ and $\lambda = 800$ nm.

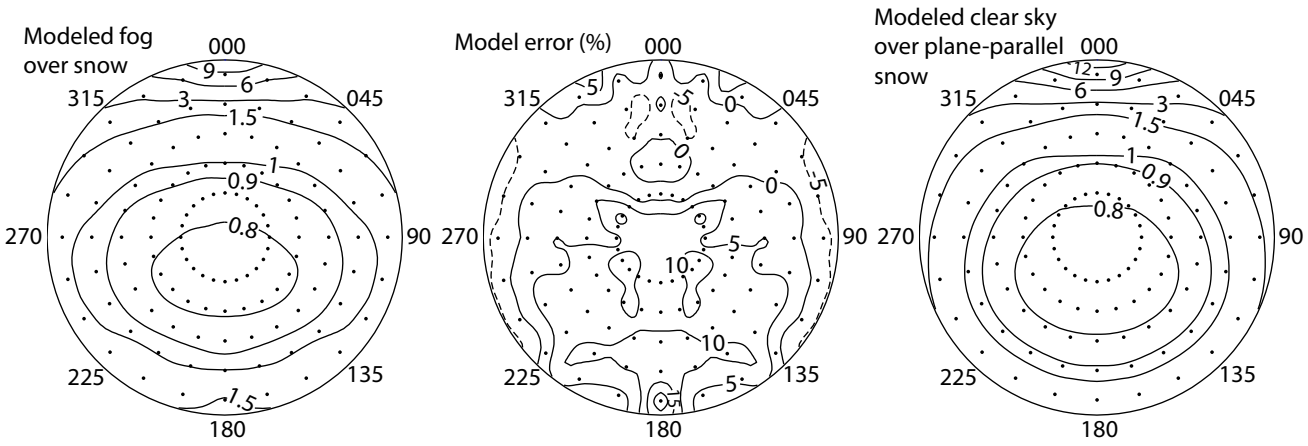

Figure 9. R modeled with DISORT for a thin, plane-parallel, liquid-water cloud immediately above a surface with the observed Dome C snow-surface BRDF, and the error of the model results relative to the fog-over-snow observation in Figure 8. Also shown is R modeled for a plane-parallel snowpack composed of rough aggregate snow grains under a clear sky. Both models used $\theta_\circ = 82.7°$ and $\lambda = 800$ nm.

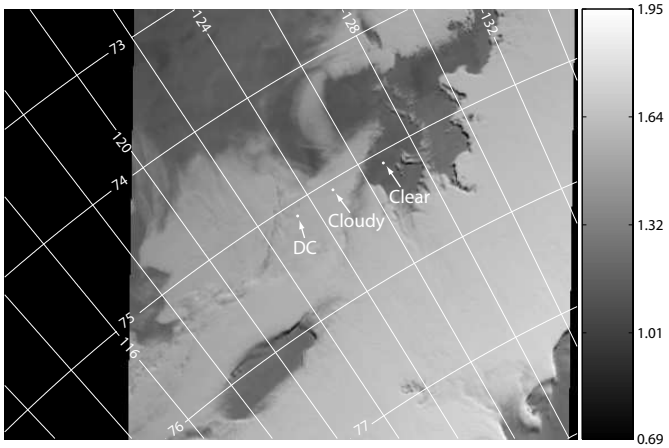

Figure 10. The BRF at 866 nm observed by MISR near Dome C at 0006 UTC 17 January 2005 at viewing zenith angle 71° and relative azimuth angle near 30°. The two marked locations in this image, one with cloud cover and one with clear sky, were chosen for further analysis (see Figure 11). A visual observation of the sky from the surface indicates it was overcast at Dome C (DC) at this time. Some surface features are visible in the clear region in the higher-resolution nadir image. The interpretation of the brighter areas as cloud and darker areas as clear is also supported by the MODIS cloud mask. The grid is labeled in degrees of south latitude and east longitude. This case uses MISR data with version number 24.

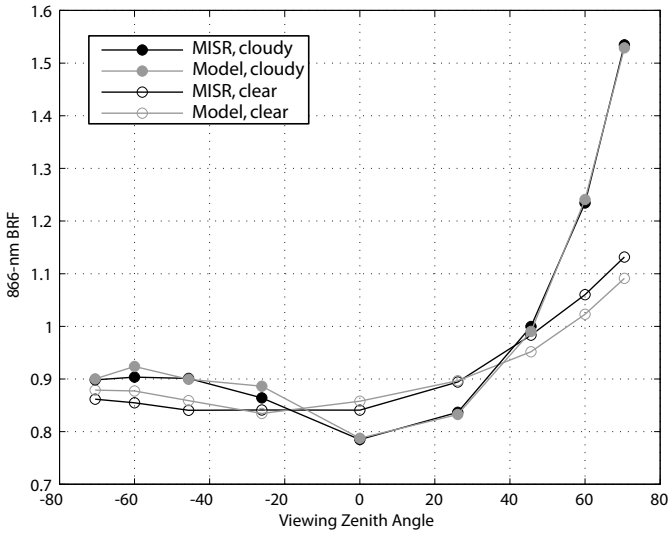

Figure 11. Observed and modeled TOA 866-nm BRF at the clear and cloudy locations marked in Figure 10. The solar zenith angle is 61.1°. The relative azimuth is about 30° for positive viewing zenith angles (forward scattering) and 150° for negative viewing zenith angles (backscattering).

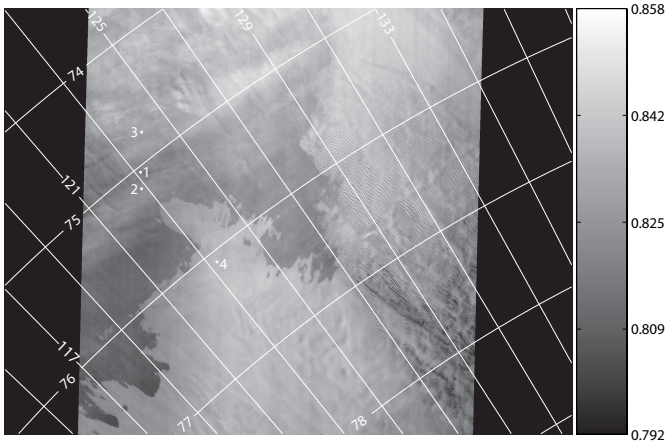

Figure 12. The near-nadir 866-nm BRF observed by MISR near Dome C at 2343 UTC 18 January 2004. The visibility of known surface features in the image and a coincident surface observation of the sky over Dome C both indicate that the sky is clear in most, if not all, of the image. The wave-like features to the right are megadunes, large-scale features on the snow surface. The magnitude of the BRF variations are small (note the scale), but, to the left, two different snow types are clearly visible. The four numbered locations correspond to the observations plotted in Figure 14. The grid is labeled in degrees of south latitude and east longitude. This case uses MISR data with version number 22.

Figure 13. View from an airplane near Siple Dome, West Antarctica (82°S, 150°W), November 1994. The surface elevation is about 500 m. The streaks which appear dark in this photograph were later identified (on an oversnow traverse by snowmobile) as surface frost; viewed from the opposite direction they instead appear brighter than the intervening regions of snow. [The frost therefore probably has little effect on the albedo.] Photo by Nadine Nereson.

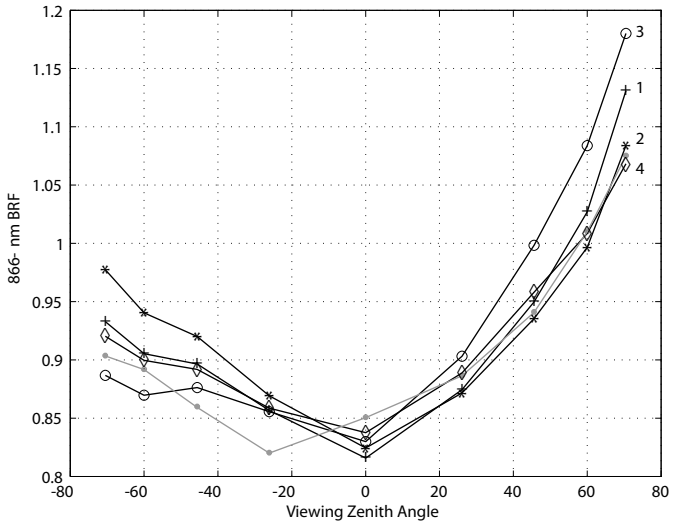

Figure 14. The four black curves show the 866-nm BRF observed by MISR at the four numbered locations in Figure 12. The gray curve is the modeled TOA 866-nm BRF. The solar zenith angle is about 63.5°.

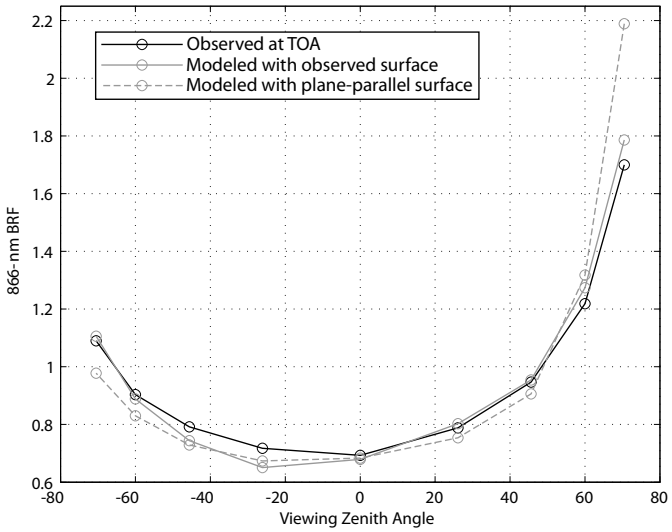

Figure 15. The observed 866-nm BRF at 1607 UTC 21 January 2004 from a clear location near Dome C is shown in black. The solid gray curve is the modeled TOA 866-nm BRF using the surface parameterization. The dashed gray curve shows the modeled BRF using a plane-parallel surface composed of aggregate ice crystals. The solar zenith angle is 85.0°.